

# **Al<sub>2</sub>MgC<sub>2</sub> and AlFe<sub>3</sub>C formation in AZ91 Mg alloy melted in Fe-C crucibles**

L. Peng<sup>a,c</sup>, G. Zeng<sup>b</sup>, C.J. Lin<sup>a</sup>, C.M. Gourlay<sup>a,d</sup>

<sup>a</sup> Department of Materials, Imperial College London, London. SW7 2AZ. UK

<sup>b</sup> School of Materials Science and Engineering, Central South University, Changsha 410083, China

<sup>c</sup> email: liuqing.peng15@imperial.ac.uk

<sup>d</sup> email: c.gourlay@imperial.ac.uk

## **Abstract**

Magnesium alloys are commonly melted and held in steel or cast iron crucibles and small but important amounts of Fe and C can dissolve into Mg-rich melts. Here, carbide formation is studied during interface reactions between solid Fe-xC alloys (x= 0 – 3.6 wt.%) and liquid Mg-9Al-0.7Zn-0.2Mn (wt.%, AZ91) at temperatures from 700 – 800 °C. Two ternary carbides, AlFe<sub>3</sub>C and Al<sub>2</sub>MgC<sub>2</sub>, formed in the reaction layers between the Fe-C and AZ91, and T2-Al<sub>2</sub>MgC<sub>2</sub> additionally formed within the AZ91 alloy due to carbon pickup. T2-Al<sub>2</sub>MgC<sub>2</sub> grew in liquid AZ91 as hexagonal plates that were commonly twinned. A reproducible orientation relationship was measured between T2-Al<sub>2</sub>MgC<sub>2</sub> and α-Mg, and the grain refinement of magnesium by heterogeneous nucleation on T2-Al<sub>2</sub>MgC<sub>2</sub> is explored.

**Keywords:** intermetallics; metals and alloys; liquid-solid reactions; microstructure; phase transitions

## **1 Introduction**

Mg alloys are commonly melted and held in carbon steel, stainless steel or cast iron crucibles owing to the low solubility of Fe in liquid Mg. However, alloying elements such as Al in AM- and AZ-series Mg alloys can react with the steel resulting in a Al-Fe(-Mn) reaction layer [1-5]. A small but important amount of Fe, meanwhile, can be picked up through the reaction layer into the melt to create Al-Mn(-Fe) IMC particles that can settle down to the bottom of crucibles and create sludge [6-8] and have a negative impact on corrosion performance if they enter the final casting.

Carbon can also be picked up from steel and cast iron crucibles. The solubility of C in liquid magnesium is approximately 20 ppm at 800 °C [9, 10] and a similar C solubility is reported for liquid AZ91 [11]. Emley [12] suggested that, during superheating, the walls of steel crucibles are decarburised resulting in carbon pickup to the Mg alloy, and that more carbon pickup occurs from new crucibles since they contain more carbon in the surface layers. When the carbon content exceeds the solubility limit of an AZ91 melt, carbides form and according to recent

thermodynamic calculations the expected carbide in Mg-9Al-0.5C (wt.%) is  $\text{Al}_2\text{MgC}_2$  [13]. For the case of carbon pickup in AZ91 from steel or cast iron crucibles, the situation is more complex with concentration gradients and Al-Fe-Mn intermetallic reaction layers. Past work has identified that Al-Fe-Mn compounds interact with carbides in Mg-Al-based alloys [14], although this has not been explored during interfacial reactions between Mg-Al-Mn alloys and Fe-C crucibles. Despite a long history of melting magnesium alloys in carbon steel and cast iron crucibles, there is little published work on how liquid Mg-Al-based alloys react with  $\text{Fe}_3\text{C}$  and graphite in these crucibles, and the extent to which carbon is picked up and forms carbides in Mg-Al alloys.

A further consideration is that carbon inoculation has been known as a grain refinement method for Mg-Al-based alloys since the 1940s [15], although the mechanism is still debated to this day [16-18]. The first hypothesis of  $\text{Al}_4\text{C}_3$  as the nucleant was proposed by Emley [12] and supported by various authors including Liu et al. [19] who grain refined AZ31/AZ63 by adding  $\text{Al}_4\text{C}_3$ -SiC/Al master alloy into the melt at 700 °C. Another hypothesis of  $\text{Al}_2\text{CO}$  was proposed by Yano et al. [20] who found an Al-C-O particle at the center of an  $\alpha$ -Mg grain. However this hypothesis was not widely accepted; for example, Lu et al. [21] pointed out that  $\text{Al}_2\text{CO}$  is likely to be unstable in a Mg-rich melt based on thermodynamic calculations. In more recent studies [22, 23],  $\text{Al}_2\text{MgC}_2$  has been proposed to be the nucleant for grain refinement of Mg-Al alloys, although this phase was found [24] and synthesised [25] back in the 1990s. In the Al-C-Mg ternary system [13, 25],  $\text{Al}_4\text{C}_3$  and  $\text{Al}_2\text{MgC}_2$  are both stable phases at 1000 K and  $\text{Al}_4\text{C}_3$  is reported to be the equilibrium phase with Mg-Al liquid only when the Al content is more than 19 wt.%. This indicates that the nucleant for grain refinement of commercial Mg-Al alloys (normally  $\leq 9$  wt.% Al) by carbon inoculation is more likely to be  $\text{Al}_2\text{MgC}_2$  ternary carbide instead of  $\text{Al}_4\text{C}_3$ . In the experiments of Huang et al. [22],  $\text{Al}_2\text{MgC}_2$  was identified by XRD in Mg-3Al alloys after the addition of SiC and a “basal-to-basal” orientation relationship (OR) between  $\text{Al}_2\text{MgC}_2$  and  $\alpha$ -Mg:  $(0001)_{\text{Al}_2\text{MgC}_2} \parallel (0001)_{\text{Mg}}$  and  $[11\bar{2}0]_{\text{Al}_2\text{MgC}_2} \parallel [11\bar{2}0]_{\text{Mg}}$ , was measured by TEM analysis. This OR was later supported by density functional theory (DFT) calculations carried out by Wang et al. [26] as the  $\alpha$ -Mg/Mg-terminated  $\text{Al}_2\text{MgC}_2$  interface shows the lowest calculated interfacial energy. However, recent papers still support different competing mechanisms (e.g.  $\text{Al}_4\text{C}_3$  clusters for nucleating  $\alpha$ -Mg [14], Al-C and Al-C/Al-Mn-(Fe) particles for nucleating  $\alpha$ -Mg inoculated by adding limestone [27], nucleation of  $\alpha$ -Mg on modified  $\text{Al}_4\text{C}_3$  in which the terminal C atoms are substituted by Mg in the melt and hence a  $\text{Al}_4\text{C}_2\text{Mg}$  interface is formed [28]) and there remains no agreement on which carbide phase causes grain refinement after carbon inoculation.

In light of the uncertainties described above, this work was performed with three primary aims: (i) to investigate how liquid Mg-9Al-0.7Zn-0.2Mn (wt.%, AZ91) reacts with carbon steel and cast iron crucibles; (ii) to identify the carbide phase(s) formed in AZ91 due to carbon pickup from these crucibles; and (iii) to explore the heterogeneous nucleation of  $\alpha$ -Mg on these carbides.

## 2 Methods

The starting material for this study was AZ91D with composition given in Table I. This alloy was studied in two forms: (1) AZ91 melted and held in Al<sub>2</sub>O<sub>3</sub> at 700 °C for 48 h to investigate pre-existing carbides in the original ingot and (2) AZ91 melted and held in Fe-0C, Fe-0.2C, Fe-1.0C and Fe-3.6C crucibles at 700-800 °C for 8 h to study the influence of C-content in the steel crucible on carbide formation. The compositions of the steels that were machined into crucibles are given in Table II. For all cases, a 2 g AZ91 cylinder was melted and held in the cylindrical crucibles with dimensions of inner diameter of 12 mm and inner height of 20 mm, within sealed quartz tubes backfilled with Ar. After the desired holding time, the samples were solidified by placing the 700 °C quartz tubes in the vertical cylindrical hole of a steel mould at room temperature. The cooling rate in the range of 700-400 °C was measured as ~4 K/s.

Table I Chemical composition of the AZ91 used in the experiment.

Alloy	Composition (wt.%)							
	Mg	Al	Zn	Mn	Cu	Si	Ni	Fe
AZ91	Bal.	8.95	0.72	0.19	0.001	0.039	<0.001	<0.001

Table II Chemical compositions of the Fe-C crucibles used in the experiment.

Alloy	Composition (wt.%)					
	Fe	C	Mn	Si	P	S
Fe-0C	Bal.	<0.02	<0.08	-	<0.02	<0.02
Fe-0.2C	Bal.	0.2	0.7	0.35	<0.05	<0.05
Fe-0.4C	Bal.	0.35	0.66	0.2	-	-
Fe-1.0C	Bal.	0.97	0.46	0.25	<0.005	<0.001
Fe-3.6C	Bal.	3.62	0.4	2.64	0.1	0.01

The microstructure of the reaction layer and carbide particles was examined by analytical scanning electron microscopy (SEM). To minimise hydrolysis of the carbide phases, cross-sections were prepared by standard metallographic procedures but with ethanol instead of water and, immediately after polishing, SEM investigation was performed using a Zeiss Sigma-300. Secondary electron (SE) and backscattered electron (BSE) images were taken with an accelerating voltage of 10 kV and a working distance of 10 mm. Energy-dispersive X-ray spectroscopy (EDS) was performed using an accelerating voltage of 10 kV, a 60-mm aperture and a working distance of 5 mm with an OXFORD X-Max detector. Electron backscattered diffraction (EBSD) was carried out using 20 kV accelerating voltage and 15 mm working distance, with a 120-mm aperture, the sample tilted at 70°, and a BRUKER e-FlashHR EBSD detector. For indexing of EBSD patterns, the phases that were considered in the Bruker

Quantax Esprit 2.1 software are listed in Table III along with their crystallographic details and references.

The reaction layer was identified further by X-ray diffraction (XRD) using a Bruker D2 Phaser diffractometer with Cu K $\alpha$  radiation ( $\lambda = 1.5418 \text{ \AA}$ ). XRD was performed on the surface of the reaction layer after  $\alpha$ -Mg was selectively etched away in 20 % nitric acid in ethanol and the subsequent surfaces after further grinding into the steel. The solid sample was rotated at 60 rpm and the diffraction data were collected in the  $2\theta$  range of  $10 - 90^\circ$  with an angular step size of  $0.02^\circ$  and 1 s integration time.

To study the  $\alpha$ -Mg grain size in AZ91, the samples were etched using a solution of 1-ml glacial acetic acid, 44-ml distilled water and 156-ml ethanol followed by imaging in an OLYMPUS SZ61 stereo-optical microscope to image the macrostructure and in an OLYMPUS BX51 optical microscope with cross-polarizer to image the colour-etched grain structure. Further details of the procedures of colour etching are given in Ref. [29].

Table III Crystal structures and lattice parameters used for analysing and indexing EBSD patterns [30-39].

Phase	Space group	Pearson symbol	Lattice parameters						ICSD collection code	Ref.
			a[ $\text{\AA}$ ]	b[ $\text{\AA}$ ]	c[ $\text{\AA}$ ]	$\alpha$ [ $^\circ$ ]	$\beta$ [ $^\circ$ ]	$\gamma$ [ $^\circ$ ]		
$\alpha$ -Mg	$P6_3/mmc$	$hP2$	3.209	3.209	5.211	90	90	120	52260	[30]
$\text{Al}_8\text{Mn}_5$	$R3mH$	$hR26$	12.601	12.601	7.931	90	90	120	254156	[31]
$\text{Al}(\text{Fe},\text{Mn})$	$Pm\bar{3}m$	$cP2$	2.910	2.910	2.910	90	90	90	165164	[32]
$\text{AlFe}_3\text{C}$	$Pm\bar{3}m$	$cP5$	3.780	3.780	3.780	90	90	90	43853	[33]
$\alpha$ -Fe	$Im\bar{3}m$	$cI2$	2.866	2.866	2.866	90	90	90	64998	[34]
$\text{Fe}_3\text{C}$	$Pnma$	$oP16$	5.081	6.753	4.515	90	90	90	99017	[35]
T1- $\text{Al}_2\text{MgC}_2$	$P6_3/mmc$	$hP10$	3.402	3.402	12.292	90	90	120	-	[36]
T2- $\text{Al}_2\text{MgC}_2$	$P\bar{3}m1$	$hP5$	3.377	3.377	5.807	90	90	120	-	[37]
$\text{Al}_4\text{C}_3$	$R\bar{3}mH$	$hR7$	3.335	3.335	24.967	90	90	120	66751	[38]
$\text{Al}_2\text{CO}$	$P6_3/mc$	$hP4$	3.200	3.200	5.100	90	90	120	250128	[39]

### 3 Results and Discussion

#### 3.1 T2-Al<sub>2</sub>MgC<sub>2</sub> pre-existing in the AZ91 ingot

Analysis of AZ91 that had been melted in Al<sub>2</sub>O<sub>3</sub> crucibles showed that some carbide particles pre-existed in the batch of AZ91 used. Fig. 1a shows a SE image of a typical particle that had settled to the bottom of an AZ91 sample in an Al<sub>2</sub>O<sub>3</sub> crucible during holding at 700 °C for 48 h. The particle contains Al, Mg and C, as shown in the EDS mapping to the right. EDS point analysis gave a composition of 33Al-21Mg-46C ( $\pm 1$  at.%), which is similar to the Al<sub>2</sub>MgC<sub>2</sub> ternary compound reported by Bosselet et al. in Ref. [25]. Fig. 1b presents EBSD analysis from the particle including a phase map and an experimental Kikuchi pattern. The EBSD pattern was auto-indexed as the T2-Al<sub>2</sub>MgC<sub>2</sub> phase by Bruker Esprit 2.1 using a Hough transform based method when all phases in Table III were used. To test this further, a dynamical simulation of the T2-Al<sub>2</sub>MgC<sub>2</sub> pattern was performed for this orientation within Bruker Esprit DynamicS and is shown at the side in Fig. 1b. The cross correlation coefficient of 0.64 indicates a good match with the experimental pattern, which can be confirmed by band-by-band inspection. More dynamical simulations and comparisons among other candidate phases (T1-Al<sub>2</sub>MgC<sub>2</sub>, Al<sub>4</sub>C<sub>3</sub>, Al<sub>2</sub>CO) are given in S.I.-Fig. 1 in the Supplementary Information, where it can be seen that only the trigonal T2-Al<sub>2</sub>MgC<sub>2</sub> structure is consistent with the experimental Kikuchi patterns from this phase. Furthermore, we note that T2-Al<sub>2</sub>MgC<sub>2</sub> is the expected equilibrium phase in AZ91 containing impurity carbon from recent work on the thermodynamics of the Al-C-Mg system [13, 40].

From Fig. 1 and other similar particles, it can be concluded that the batch of ‘high purity’ AZ91 used in this study (Table I) contained pre-existing T2-Al<sub>2</sub>MgC<sub>2</sub> particles that are stable at 700 °C. Presumably, this was caused by a sufficiently high impurity-carbon content in the commercial AZ91 ingot. To our knowledge, this is the first observation of T2-Al<sub>2</sub>MgC<sub>2</sub> particles in AZ91 (without the addition of SiC [22] or synthesis by slow evaporation of Mg [25, 37]). The possibility of finding these particles in this study was increased by the experimental method used, where gravity-driven sedimentation concentrated the particles at the bottom of the AZ91 samples, and the 48 h holding period is likely to have coarsened the particles to a size suitable for analytical SEM.

## 3.2 Influence of C-content in the steel crucible on carbide formation

### 3.2.1. Summary of key features

Fig. 2 overviews the typical microstructures of AZ91 and the reaction layers after holding in different Fe and Fe-C crucibles (Fe-0C, Fe-0.2C, Fe-1.0C and Fe-3.6C) for 8 h at 700 °C. Fig. 2a are low magnification images highlighting the main microstructural features in AZ91; the Mn-bearing intermetallic (IMC) particles and eutectic  $\text{Mg}_{17}\text{Al}_{12}$  in an  $\alpha$ -Mg matrix. Between the Mg matrix and the crucibles, a continuous IMC reaction layer can also be observed.

Fig. 2b exhibits the detailed microstructures of the IMC reaction layers in pure Fe, Fe-0.2C, Fe-1.0C and Fe-3.6C crucibles at the same magnification. It can be seen that there are numerous thin dark vertical plates present in the reaction layer for the Fe-0.2C, Fe-1.0C and Fe-3.6C crucibles, whereas these plates are absent in the pure Fe crucible. The cast iron additionally contains flake graphite and some graphite penetrates through the reaction layer into the  $\alpha$ -Mg matrix. In the region of  $\alpha$ -Fe towards the bottom of each image, the number of eutectoid  $\text{Fe}_3\text{C}$  particles (small bright particles) increases from the Fe-0.2C to Fe-1.0C crucibles. Ahead of the interface in the bulk AZ91, the carbide particles also increase significantly with the ascending carbon content. It is also noticeable that there is a thin layer present between the reaction layer (containing dark vertical plates) and the  $\alpha$ -Fe beneath in the Fe-0.2C, Fe-1.0C and Fe-3.6C crucibles. These microstructural features are explored in detail in the next sections.

### 3.2.2 Carbide formation in Fe-C crucibles

Fig. 3 is a typical region of reaction layer for AZ91 held in Fe-1.0C for 8 h at 700 °C. Fig. 3a shows a phase map from EBSD analysis. It can be seen that the main reaction layer is B2-Al(Fe,Mn) (i.e. with CsCl structure, Table III) which contains dark plates of T2- $\text{Al}_2\text{MgC}_2$  carbide, although only a small fraction of those carbides were indexed in Fig. 3a due to their small dimensions. A layer of  $\text{Al}_8\text{Mn}_5$  was indexed on top of the B2 layer, which likely formed during cooling. Between the B2 and  $\alpha$ -Fe, there is a thin layer of  $\kappa$ - $\text{AlFe}_3\text{C}$ .

In this reaction zone, three types of carbide could be clearly distinguished, T2- $\text{Al}_2\text{MgC}_2$  ternary carbide in the Mg bulk,  $\kappa$ - $\text{AlFe}_3\text{C}$  between the B2 layer and  $\alpha$ -Fe, and cementite  $\text{Fe}_3\text{C}$  in the underlying steel. Their experimental Kikuchi patterns are shown in Fig. 3a with dynamical simulated patterns for each orientation beneath. Band by band inspection and the high cross correlation coefficients indicate good agreement with the experimental patterns. Combining all the features above, the complex microstructure of the reaction layer is drawn schematically in Fig. 3b.

To further confirm the identity of the A2- $\alpha$ -Fe, B2-Al(Fe,Mn) and  $\text{Al}_8\text{Mn}_5$ , XRD was performed on the reaction layers in three stages. First after selective etching of the  $\alpha$ -Mg revealing the top of the reaction layer. Next after a first grinding step through the top of the reaction layer, and then a second grinding step to beneath the reaction layer. XRD results are presented in Fig. 3c. The second grinding step gave single-phase A2- $\alpha$ -Fe with the three

fundamental reflections in the range  $2\theta=10-90^\circ$  corresponding to disordered BCC. The first grinding layer contained single-phase B2-Al(Fe,Mn) with clear ordered superstructure peaks in addition to the fundamental reflections. Note that the T2-Al<sub>2</sub>MgC<sub>2</sub> plates were reacted during sample preparation leaving only B2-Al(Fe,Mn). The top ‘as-etched’ step contained a two-phase mixture of B2-Al(Fe,Mn) and Al<sub>8</sub>Mn<sub>5</sub>. Higher magnification images of the XRD patterns and further information on the peaks are given in S.I.-Fig. 2-4 in the Supplementary Information.

Fig. 4a shows EDS analysis on a region near the  $\kappa$ -AlFe<sub>3</sub>C layer in a Fe-0.2C crucible to present the dark plate phase in the B2 layer in more detail. The microstructure of this region is illustrated in the schematic in Fig. 4b. From the EDS mapping, it can be clearly seen that the plate carbide in the B2 layer contains Mg, C and Al, providing further evidence that this is an Al-Mg-C ternary carbide. The EDS mapping also confirms the presence of Al, Fe, C in the  $\kappa$ -AlFe<sub>3</sub>C layer, Al and Fe in the B2-Al(Fe,Mn) phase, and Fe in the  $\alpha$ -Fe phase. Note that Mn is not shown as an EDS map as Fe is dominant in this region near the bottom of the reaction layer (the composition of the B2 phase here is 46Al-1Mn-53Fe ( $\pm 1$  at.%)).

To further understand the plate carbide within the B2-Al(Fe,Mn) layer, AZ91 held in cast iron crucibles (Fe-3.6C) was studied where there is a higher volume fraction of carbides. Fig. 5a and b show the typical microstructure of the reaction layer between AZ91 and a 3.6 wt.% C cast iron crucible after isothermal holding at 700 °C for 8 h. Fig. 5a shows SE imaging and EDS mapping of a region containing a graphite flake in the B2 layer. In the SE image, the darkest phase is graphite and it is transforming into grey plates attached to it. These plates contain C, Al and Mg in the EDS maps in Fig. 5a, consistent with an Al-Mg-C ternary carbide. Fig. 5b is a schematic summarising the key features of Fig. 5a.

Fig. 5c is EBSD analysis of a transforming graphite flake in the B2 layer. Note that the ternary carbides have grown to a sufficient size to be indexed when compared to the small plates in Fig. 4a. The graphite was not indexed since it did not give any Kikuchi patterns, however a T2-Al<sub>2</sub>MgC<sub>2</sub> carbide was indexed with the experimental Kikuchi pattern shown to the right. A dynamical simulation shows a cross correlation coefficient of 0.49 to the experimental pattern (Fig. 5c). This relatively low value is due to the lower quality Kikuchi pattern than others in this paper; in this case, band-by-band inspection of the experimental and simulated Kikuchi patterns can be used to further confirm the good match to T2-Al<sub>2</sub>MgC<sub>2</sub>. Meanwhile, other regions of ternary carbide as identified in the EDS maps of Fig. 5a were not indexed in Fig. 5c because no Kikuchi pattern was detected in these regions. There was some evidence that certain regions of carbide in the B2 layer were sensitive to the electron beam (transforming under the e-beam), and it is possible that the beam-sensitive carbide is the T1-Al<sub>2</sub>MgC<sub>2</sub> identified in Bosselet’s experiments [25], but this could not be confirmed.

Combining the results in Figures 2-5 it can be concluded that, for holding liquid AZ91 in Fe-C crucibles at 700 °C, Mg and Al from liquid AZ91 react with carbon in the steel/cast iron to form plates of T2-Al<sub>2</sub>MgC<sub>2</sub> ternary carbide in a two-phase reaction layer of B2+Al<sub>2</sub>MgC<sub>2</sub>. Examining Fig. 2, note that the B2+Al<sub>2</sub>MgC<sub>2</sub> reaction layer is approximately 10-20  $\mu\text{m}$  thick (after 8 h at 700 °C) and is adhered to the crucible surface so a significant fraction of T2-

$\text{Al}_2\text{MgC}_2$  reaction product develops in the surface layer of the steel rather than in the AZ91 melt. However, since these experiments were conducted under quiescent conditions without stirring or pouring, it is unclear to what extent this layer could detach/fracture/spall and enter the liquid AZ91 during industrial melt handling.

### 3.2.3 The $\kappa$ - $\text{AlFe}_3\text{C}$ layer

Fig. 6a shows a typical microstructure of the  $\kappa$ - $\text{AlFe}_3\text{C}$  layer formed in AZ91 held in a Fe-1.0C steel crucible at 700 °C for 8 h and a deep-etched sample tilted at 54° revealing the 3-D microstructure around the  $\kappa$ - $\text{AlFe}_3\text{C}$  layer. The  $\kappa$ - $\text{AlFe}_3\text{C}$  layer separates a region containing B2-Al(Fe,Mn) +  $\text{Al}_2\text{MgC}_2$  plates above and A2- $\alpha$ -Fe + coarsened  $\text{Fe}_3\text{C}$  particles below. Note in the deep-etched sample, the  $\text{Al}_2\text{MgC}_2$  plates have reacted and they can be seen from the plate shaped holes. Fig. 6b shows EBSD analysis of the  $\kappa$ - $\text{AlFe}_3\text{C}$  layer. The inverse pole figure (IPF-X) map shows that the layer is a single-grain thick and comprised of numerous equiaxed  $\kappa$ - $\text{AlFe}_3\text{C}$  grains without any apparent preferred texture. The measurement of the grain size along the layer length and the layer thickness in different experimental conditions is plotted in Fig. 6c. It can be seen that, at 700 °C, the lateral grain size of  $\kappa$ - $\text{AlFe}_3\text{C}$  seems to saturate at a maximum of ~1  $\mu\text{m}$ , while the  $\kappa$ - $\text{AlFe}_3\text{C}$  layer thickness keeps increasing with time and C-content. Elevating the temperature to 800 °C (for the Fe-3.6C cast iron), the grain size increased to ~3.5  $\mu\text{m}$ , while remaining a single-grain thick. 0 out of 32  $\kappa$ - $\text{AlFe}_3\text{C}$  grains was found to have a simple or reproducible OR with the adjacent  $\alpha$ -Fe or B2-Al(Fe,Mn) grains via EBSD analysis. Similarly, 0 out of 26  $\text{Fe}_3\text{C}$  particles attached/adjacent to the  $\kappa$ - $\text{AlFe}_3\text{C}$  phase had a simple and reproducible OR with  $\kappa$ - $\text{AlFe}_3\text{C}$ .

The presence of a  $\kappa$ - $\text{AlFe}_3\text{C}$  layer was found to depend on the combination of the carbon content in the Fe-C crucible and the holding temperature as summarised in Table IV.

Table IV Summary of conditions where a  $\kappa$ - $\text{AlFe}_3\text{C}$  layer formed. ✓ =  $\kappa$ - $\text{AlFe}_3\text{C}$  layer present. x =  $\kappa$ - $\text{AlFe}_3\text{C}$  layer not found. - = not studied.

Holding T [°C]	C content in crucible [wt.% C]				
	0	0.2	0.4	1.0	3.6
700	x	✓	✓	✓	✓
750	-	✓	-	-	-
800	-	x	-	-	✓

Fig. 7 displays the reaction layers and diffusion profiles in Fe-0.2C steel crucibles after holding at 700 °C where a  $\kappa$ - $\text{AlFe}_3\text{C}$  layer formed, and at 800 °C where one did not (Table IV). Fig. 7a shows SEM images, EDS mapping and an EBSD phase map of the reaction layers. Fig. 7b is the diffusion profile for the reaction layers which has been colour indexed by the phases identified in the EBSD phase map. From the EDS mapping in Fig. 7a, it can be seen that a carbon-rich layer is present in the 700 °C sample but not in 800 °C, which corresponds to  $\kappa$ -



AlFe<sub>3</sub>C identified through EBSD analysis. It also can be seen in Fig. 7b, that for 700 °C, the Al content has a steady composition ~45-50 at.% in the B2 layer and a step change to ~20 at.% in  $\kappa$ -AlFe<sub>3</sub>C and <0.1 at.% in the underlying steel. In contrast, in the 800 °C sample the Al content has a gradual change from ~45 to 0 at.% across the whole reaction layer. This indicates that the  $\kappa$ -AlFe<sub>3</sub>C layer acts as a barrier to Al diffusion from the AZ91 into the steel, at the phase boundary of B2 and A2. Due to the absence of a  $\kappa$ -AlFe<sub>3</sub>C layer in the 800 °C sample, a schematic is drawn in Fig. 7a to illustrate the layer structure at 800 °C where the position of the B2/A2 boundary has been estimated from the Al content.

To interpret the presence or absence of a  $\kappa$ -AlFe<sub>3</sub>C layer and the diffusion profiles for varying holding temperatures and steel compositions, it is useful to mark the information in Table IV and Fig. 7 on the Fe-rich corner of ternary Al-C-Fe isothermal sections. Fig. 8 is a plot of the partial Al-C-Fe isothermal sections at 700, 750 and 800 °C from the Thermo-Calc TCFE7.0 database. The Fe-rich regions are expanded to the left of each section to highlight the initial steel compositions and the regions where FCC  $\gamma$ -Fe is stable. Solid red circles indicate initial steel compositions for which a  $\kappa$ -AlFe<sub>3</sub>C layer formed during reaction with AZ91 at that temperature. Unfilled red circles indicate initial steel compositions for which a  $\kappa$ -AlFe<sub>3</sub>C did not form.

It can be seen that a  $\kappa$ -AlFe<sub>3</sub>C layer formed (filled red circles) for all composition-temperature combinations where graphite (or Fe<sub>3</sub>C) was present in the initial steel at the holding temperature (i.e. when the initial composition lies on a BCC+G or FCC+G tie line). When the initial steel contained BCC+FCC at the holding temperature (i.e. when all carbon was initially dissolved, mostly in FCC-Fe, in the initial steel), a  $\kappa$ -AlFe<sub>3</sub>C layer formed at 750°C but not at 800°C (open red circles). In the 750 °C isothermal section, FCC ( $\gamma$ -Fe) is only stable up to ~0.3 at.% Al and it may be that enough Al diffused into the steel early in the experiment to exceed the local Al solubility in FCC-Fe and enable the formation of BCC- $\alpha$ -Fe and a carbide. In contrast, at 800 °C the FCC ( $\gamma$ -Fe) region has significantly higher solubility for Al and all carbon may have diffused and dissolved into FCC before enough Al had diffused into the steel at 800 °C. Another factor is that there is the higher solubility of C in liquid AZ91 at 800 °C which could have partially decarburised the steel surface region. The composition data from Fig. 7b are plotted as blue diamonds on the 800 °C Al-C-Fe isothermal section in Fig. 8. Since no carbide phase was detected in this region, the diffusion path just follows the Al-Fe binary side as the Al dissolves into the steel.

For the case at 700°C, the diffusion profile and  $\kappa$ -AlFe<sub>3</sub>C layer (Fig. 7b) can be understood from the 700°C isothermal section in Fig. 8. Although the composition measurements are not sufficiently closely spaced to deduce the precise diffusion path, the following can be reasonably inferred from the EDS datapoints (blue diamonds) on the 700 °C isothermal section: The steel begins in the BCC- $\alpha$ Fe plus graphite (or Fe<sub>3</sub>C) two phase region with no dissolved Al. As the Al diffuses into the steel, the Al content in the BCC phase increases until it reaches the solubility limit of ~7 wt.% Al at which point we enter the BCC + C +  $\kappa$ -AlFe<sub>3</sub>C three-phase region and a  $\kappa$ -AlFe<sub>3</sub>C layer is present. On the other side of the  $\kappa$ -AlFe<sub>3</sub>C layer, we enter the three-phase region of  $\kappa$ -AlFe<sub>3</sub>C+ BCC+ Al<sub>4</sub>C<sub>3</sub> where there is ~20 wt.% Al in the BCC phase.

The calculation gives  $\text{Al}_4\text{C}_3$  because we have approximated the system as the Al-C-Fe ternary (without Mg, Mn or Zn) whereas, in reality, there is likely to be a BCC +  $\text{Al}_2\text{MgC}_2$  two-phase (or higher order) mixture at this location. With continued diffusion of Al, the composition of the BCC phase increases in the BCC+  $\text{Al}_4\text{C}_3$  two phase region (BCC +  $\text{Al}_2\text{MgC}_2$  in reality), exceeding 30 wt.% Al. At this point, we are approaching the interface with liquid AZ91, where the Mn content becomes significant (Fig. 7b), and the Al-C-Fe ternary is no longer a reasonable approximation of the multicomponent diffusion couple. In the isothermal sections, note that ordering (i.e. A2 versus B2) is not taken into consideration.

Similar results have been reported in studies of Fe-C alloys hot dipped in liquid Al and Al-based alloys at temperatures in the range 600-950 °C [41-44], although the main intermetallic reaction layer is  $\eta\text{-Al}_5\text{Fe}_2$  (instead of B2-AlFe) in those more Al-rich systems. In Kwak et al.'s experiment [44], Fe-0.23C steel was hot dipped in liquid Al-7Mn alloy at 773 °C up to 120 s and a  $\kappa\text{-AlFe}_3\text{C}$  layer was found between  $\eta\text{-Al}_5\text{Fe}_2$  and A2- $\alpha\text{-Fe}$ . In Sidhu et al.'s experiment [42], cast iron (~3 wt.% C) was hot dipped in liquid Al (99.97 wt.%) at 950 °C for 2 h and a  $\kappa\text{-AlFe}_3\text{C}$  layer was formed between B2-AlFe (a thin layer adjacent to  $\eta\text{-Al}_5\text{Fe}_2$ ) and A2- $\alpha\text{-Fe}$ . In addition to  $\kappa\text{-AlFe}_3\text{C}$  carbide, lath shaped  $\text{Al}_4\text{C}_3$  particles with was also identified in B2 layer which is consistent with the prediction in the Al-Fe-C isothermal sections in Fig. 8 without the involvement of Mg. In other experiments [41, 43], a  $\kappa\text{-AlFe}_3\text{C}$  layer was also found between B2-AlFe and A2- $\alpha\text{-Fe}$  in the temperature range of 600-690 °C for low carbon steels (<0.2 wt.% C). Despite the reaction layer(s), which depends on the Al-content in the liquid alloy and reaction time, their results are comparable with the present work, although this is the first observation of a  $\kappa\text{-AlFe}_3\text{C}$  layer in a Mg-Al alloy in contact with Fe-C alloys, and the  $\kappa\text{-AlFe}_3\text{C}$  layer shows a barrier effect on preventing Al diffusion into the steel crucible.

### 3.3 Growth crystallography of $\text{Al}_2\text{MgC}_2$

T2- $\text{Al}_2\text{MgC}_2$  additionally formed as isolated particles within the AZ91 alloy due to carbon pickup. The growth facet of these T2- $\text{Al}_2\text{MgC}_2$  crystals could be deduced using SE imaging and EBSD analysis on 2-dimensional cross-sections. Fig. 9a shows a SE image of a T2- $\text{Al}_2\text{MgC}_2$  particle containing clear facets, and the unit cell orientation of the crystal is plotted using the Euler angles measured by EBSD. Digitally sectioning the wireframe unit cell in the plane of the SE image produced the orange geometry. The similarity between the facet geometry in the SE image and the orange section of the wireframe unit cell identifies the facet as  $\{0001\}$ . Analysis of multiple such crystals showed that T2- $\text{Al}_2\text{MgC}_2$  often grew with a layered structure, with layers parallel to  $\{0001\}$  as in the example in Fig. 9a. This layered structure was often associated with growth twinning.

In Fig. 9a, the IPF-Z orientation map shows two orientations (green and blue) with a linear interface in the particle. The Kikuchi patterns from the 'green' and 'blue' regions along with dynamical simulations of these orientations are attached to the right. Selected members of  $\{0001\}$ ,  $\{11\bar{2}0\}$  and  $\langle 1\bar{1}00 \rangle$  are indexed on the Kikuchi patterns to highlight two parallel planes and a parallel direction in the two patterns.

Fig. 9b shows the orientation relationship in more detail using pole figures. It can be seen that the  $\{0001\}$  and  $\{11\bar{2}0\}$  families are all overlapped at each spot and the  $\{10\bar{1}1\}$  do not overlap. The pole figures show a  $60^\circ$  rotation around a common  $[0001]$  axis. Adjacent to the pole figures, the wireframe unit cells and the atomic arrangement within the unit cells are plotted from the EBSD-measured Euler angles for the two orientations. Note that the two hexagonal wireframes have an equivalent orientation but the Al and C atoms within the unit cells are oriented differently. This can be understood from the view along  $[0001]$  in Fig. 9c: T2- $\text{Al}_2\text{MgC}_2$  has only three-fold rotation symmetry around  $[0001]$  and a  $60^\circ$  rotation about  $[0001]$  brings the Al and C atoms to inequivalent positions but the Mg atoms (vertex atoms) to equivalent positions. From the layered structure in the SE image of Fig. 9a, and the pole figures and unit cell orientations in Fig. 9b, it can be deduced that the composition plane is  $\{0001\}$ , most likely consisting of Mg atoms, and the twinned orientations are related by a  $60^\circ$  rotation around the  $[0001]$  axis.

### 3.4 Nucleation of $\alpha$ -Mg on T2-Al<sub>2</sub>MgC<sub>2</sub>

The presence of an increased fraction of T2-Al<sub>2</sub>MgC<sub>2</sub> in the bulk AZ91 indicates that C-pickup from the crucible occurred in the AZ91 melt. However, as shown in Fig. 10, no grain refinement occurred when a Fe-3.6C crucible was used compared with a Fe-0C crucible at either 700 or 800 °C holding temperature. The measured grain size from linear intercept method is given in Table V.

Table V Measured grain size of AZ91 in Fe-0C and Fe-3.6C at 700 and 800 °C.

	Fe-0C [ $\mu\text{m}$ ]	Fe-3.6C [ $\mu\text{m}$ ]
700 °C	202 $\pm$ 7	243 $\pm$ 8
800 °C	126 $\pm$ 4	172 $\pm$ 9

Despite the lack of grain refinement, the settled T2-Al<sub>2</sub>MgC<sub>2</sub> particles were commonly found to have an orientation relationship (OR) with the surrounding  $\alpha$ -Mg. Since the T2-Al<sub>2</sub>MgC<sub>2</sub> were present above the  $\alpha$ -Mg liquidus, this indicates that  $\alpha$ -Mg nucleated on T2-Al<sub>2</sub>MgC<sub>2</sub>. An example is given in Fig. 11a which shows a large T2-Al<sub>2</sub>MgC<sub>2</sub> particle (~18  $\mu\text{m}$  long) in AZ91 near the bottom of the sample. The elemental distribution was identified by EDS mapping shown at the right, and EDS point analysis gave a composition of 34Al-19Mg-47C ( $\pm$ 1 at.%). The layered structure parallel to {0001} can be observed more clearly in this particle. Fig. 11b shows that this particle was twinned during growth and the EBSD patterns of the surrounding  $\alpha$ -Mg and the T2 particle are shown with and without indexing. It can be seen that the  $\alpha$ -Mg and both T2-Al<sub>2</sub>MgC<sub>2</sub> orientations share the parallel planes of {0001} and {11 $\bar{2}$ 0}, and common  $\langle$ 11 $\bar{2}$ 0 $\rangle$  and  $\langle$ 1 $\bar{1}$ 00 $\rangle$ -type directions.

The OR with  $\alpha$ -Mg and twinning of T2-Al<sub>2</sub>MgC<sub>2</sub> can also be identified in the pole figures in Fig. 11c. In the {0001} and {11 $\bar{2}$ 0} pole figures, the two orientations (colours) in T2-Al<sub>2</sub>MgC<sub>2</sub> overlap each other and also overlap with the  $\alpha$ -Mg at each spot. Note that the colours for the two orientations of T2-Al<sub>2</sub>MgC<sub>2</sub> in the pole figures have been replaced by blue and red, as marked in the IPF-Z map, for better visual recognition. In the {10 $\bar{1}$ 1} pole figure, the two orientations (colours) in T2-Al<sub>2</sub>MgC<sub>2</sub> do not overlap each other after 60° rotation due to the three-fold symmetry of this trigonal crystal, but overlap with three spots each in the {10 $\bar{1}$ 1} of hexagonal  $\alpha$ -Mg. Together, the six spots of {10 $\bar{1}$ 1} in T2-Al<sub>2</sub>MgC<sub>2</sub> overlap with the {10 $\bar{1}$ 1} in  $\alpha$ -Mg. The crystal orientations and symmetry can be seen in the unit cells attached to the right of pole figures and the projection views in Fig. 11d. Note that, along [0001] of each crystal, hexagonal  $\alpha$ -Mg has a six-fold 6<sub>3</sub> screw axis whereas trigonal T2-Al<sub>2</sub>MgC<sub>2</sub> has only a three-fold rotation axis. Both twinned orientations of T2-Al<sub>2</sub>MgC<sub>2</sub> have an equivalent OR with  $\alpha$ -Mg which can be written:

$$(0001)_{\alpha\text{-Mg}} \parallel (0001)_{\text{T2-Al}_2\text{MgC}_2} \text{ and } [11\bar{2}0]_{\alpha\text{-Mg}} \parallel [11\bar{2}0]_{\text{T2-Al}_2\text{MgC}_2}$$

Considering that the main facet of T2-Al<sub>2</sub>MgC<sub>2</sub> in SE images is (0001) and the closest planar match between  $\alpha$ -Mg and T2-Al<sub>2</sub>MgC<sub>2</sub> is basal-on-basal, it is likely that the interface plane

within the OR is (0001). As can be seen in Table III, the 'a' lattice parameter of  $\alpha$ -Mg and T2- $\text{Al}_2\text{MgC}_2$  differs by ~5%, giving a planar mismatch in the basal plane of ~5%. The measured OR is the same as that reported by Huang et al. [22] between  $\alpha$ -Mg and  $\text{Al}_2\text{MgC}_2$  in SiC-inoculated AZ91. This OR and interface has also been studied by first-principles calculations [26] where it was shown that the interface between basal  $\alpha$ -Mg and Mg-terminated basal  $\text{Al}_2\text{MgC}_2$  is the most likely surface for nucleation of  $\alpha$ -Mg on  $\text{Al}_2\text{MgC}_2$  particles due to its lowest interfacial energy.

The lack of grain refinement in the AZ91 samples in Fig. 10 is probably due to the experimental approach used in this work. The T2- $\text{Al}_2\text{MgC}_2$  particles were large and mostly settled to the bottom of the crucibles (as can be seen in Fig. 2b) due to the long holding time of 8 h without stirring or pouring and were, therefore, not dispersed in the melt. The small sample size (12mm diameter) and relatively fast cooling rate may also have played a role. However, it seems likely that nucleation of  $\alpha$ -Mg on T2- $\text{Al}_2\text{MgC}_2$  could be optimised by adjusting the number density, size distribution and dispersion of particles in the melt in future work.

## 4 Conclusions

The formation of carbides has been investigated during reactions between solid Fe-xC alloys (x= 0 - 3.6 wt.%) and liquid Mg-9Al-0.7Zn-0.2Mn (wt.%, AZ91).

The ternary carbide  $\kappa$ -AlFe<sub>3</sub>C formed as a thin reaction layer between the  $\alpha$ -Fe and an ordered B2-Al(Fe,Mn) reaction layer due to diffusion of Al from the AZ91 into the Fe-C. Once formed, the  $\kappa$ -AlFe<sub>3</sub>C layer acted as a diffusion barrier preventing Al diffusion deeper into the Fe-C alloys.

The ternary carbide T2-Al<sub>2</sub>MgC<sub>2</sub> formed both in the upper regions of the reaction layer near the steel surface and within the bulk AZ91 due to carbon pickup from the crucible. When formed in the liquid AZ91, trigonal Al<sub>2</sub>MgC<sub>2</sub> grew as platelets with (0001) as the major facet and commonly developed growth twins with a (0001) composition plane and two orientations related by a 60° rotation around the common [0001]. The presence of a settled layer of T2-Al<sub>2</sub>MgC<sub>2</sub> did not cause grain refinement of AZ91, but settled large T2-Al<sub>2</sub>MgC<sub>2</sub> particles often had the following orientation relationship with the surrounding  $\alpha$ -Mg:

$$(0001)_{\alpha-Mg} \parallel (0001)_{T2-Al_2MgC_2} \text{ and } [11\bar{2}0]_{\alpha-Mg} \parallel [11\bar{2}0]_{T2-Al_2MgC_2}$$

This indicates that T2-Al<sub>2</sub>MgC<sub>2</sub> is a heterogeneous nucleant for  $\alpha$ -Mg but it is not an effective grain refiner when present as a settled layer. A small amount of T2-Al<sub>2</sub>MgC<sub>2</sub> particles were found pre-existing in the initial commercial AZ91 ingot and further pickup from the crucible increased the amount of Al<sub>2</sub>MgC<sub>2</sub> in AZ91.

While past workers, including Emley [12], have suggested that carbon pickup from steel crucibles produces Al<sub>4</sub>C<sub>3</sub> in AZ91, Al<sub>4</sub>C<sub>3</sub> was not detected in this work and the only carbide detected in AZ91 was T2-Al<sub>2</sub>MgC<sub>2</sub>.

## Acknowledgements

The authors gratefully acknowledge the use of characterisation facilities within the Harvey Flower Electron Microscopy Suite, Department of Materials, Imperial College London. This work was partially funded by the UK EPSRC Future LiME Hub (EP/N007638/1).

## References

- [1] F. Czerwinski, Corrosion of materials in liquid magnesium alloys and its prevention, *Magnesium Alloys—Properties in Solid and Liquid States*, (2014) 131-170.
- [2] J.C. Viala, D. Pierre, F. Bosselet, M. Peronnet, J. Bouix, Chemical interaction processes at the interface between mild steel and liquid magnesium of technical grade, *Scripta materialia*, 40 (1999).
- [3] M. Nave, A. Dahle, D. StJohn, Method for determining reaction rate of mild steel containers during melting of magnesium-aluminium alloys and effect of aluminium content on directionally solidified microstructures, *International Journal of Cast Metals Research*, 16 (2003) 427-433.
- [4] T. Ohmi, M. Iguchi, Bonding Strengths of Interfaces between Cast Mg-Al Alloy and Cast-In Inserted Transition Metal Cores, *Journal of the Japanese Society for Experimental Mechanics*, 13 (2013) s189-s193.
- [5] C. Scharf, A. Ditze, Iron pickup of AZ91 and AS31 magnesium melts in steel crucibles, *Advanced Engineering Materials*, 9 (2007) 566-571.
- [6] A. Thorvaldsen, D. Albright, Sludge in Magnesium Die Casting, in: 17 th International Die Casting Congress and Exposition, 1993, pp. 337-340.
- [7] C. Corby, N. Ricketts, M. Qian, R. Bailey, Investigation of intermetallics in magnesium die-casting sludge, *Magnes. Technol.*, (2004) 209-214.
- [8] L. Peng, G. Zeng, T. Su, H. Yasuda, K. Nogita, C. Gourlay, Al 8 Mn 5 Particle Settling and Interactions with Oxide Films in Liquid AZ91 Magnesium Alloys, *JOM*, 71 (2019) 2235-2244.
- [9] H.-L. Chen, N. Li, A. Klostermeier, R. Schmid-Fetzer, Measurement of carbon solubility in magnesium alloys using GD-OES, *Journal of Analytical Atomic Spectrometry*, 26 (2011) 2189-2196.
- [10] H.-L. Chen, R. Schmid-Fetzer, The Mg–C phase equilibria and their thermodynamic basis, *International journal of materials research*, 103 (2012) 1294-1301.
- [11] E. Bobalek, S. Shrader, Determination of Hydrogen, Carbon, and Nitrogen in Magnesium Alloys, *Industrial & Engineering Chemistry Analytical Edition*, 17 (1945) 544-553.
- [12] E.F. Emley, *Principles of magnesium technology*, (1966).
- [13] G. Deffrennes, B. Gardiola, M. Lomello-Tafin, A. Pasturel, A. Pisch, J. Andrieux, R. Schmid-Fetzer, O. Dezellus, Thermal stability of Al<sub>2</sub>MgC<sub>2</sub> and thermodynamic modeling of the Al–C–Mg system-Application to grain refinement of Mg–Al alloys, *Calphad*, 67 (2019) 101678.
- [14] M. Han, X. Zhu, T. Gao, X. Liu, Revealing the roles of Al<sub>4</sub>C<sub>3</sub> and Al<sub>8</sub>Mn<sub>5</sub> during  $\alpha$ -Mg nucleation in Mg-Al based alloys, *Journal of Alloys and Compounds*, 705 (2017) 14-21.
- [15] C.E. Nelson, Grain size behavior in magnesium casting alloys, *Trans AFS*, 56 (1948) 1e23.
- [16] D. StJohn, M. Easton, M. Qian, J. Taylor, Grain refinement of magnesium alloys: a review of recent research, theoretical developments, and their application, *Metallurgical and materials transactions A*, 44 (2013) 2935-2949.
- [17] Y. Ali, D. Qiu, B. Jiang, F. Pan, M.-X. Zhang, Current research progress in grain refinement of cast magnesium alloys: a review article, *Journal of Alloys and Compounds*, 619 (2015) 639-651.
- [18] E. Karakulak, A review: Past, present and future of grain refining of magnesium castings, *Journal of Magnesium and Alloys*, 7 (2019) 355-369.
- [19] Y. Liu, X. Liu, B. Xiufang, Grain refinement of Mg–Al alloys with Al<sub>4</sub>C<sub>3</sub>–SiC/Al master alloy, *Materials Letters*, 58 (2004) 1282-1287.
- [20] E. Yano, Y. Tamura, T. Motegi, E. Sato, Effect of carbon powder on grain refinement of an AZ91E magnesium alloy, *Materials Transactions*, 44 (2003) 107-110.
- [21] L. Lu, A. Dahle, D. StJohn, Heterogeneous nucleation of Mg–Al alloys, *Scripta Materialia*, 54 (2006) 2197-2201.
- [22] Y. Huang, K.U. Kainer, N. Hort, Mechanism of grain refinement of Mg–Al alloys by SiC inoculation, *Scripta Materialia*, 64 (2011) 793-796.
- [23] G. Deffrennes, B. Gardiola, M. Lomello, J. Andrieux, O. Dezellus, R. Schmid-Fetzer, Thermodynamics of Phase Formation in Mg–Al–C Alloys Applied to Grain Refinement, in: *TMS Annual Meeting & Exhibition*, Springer, 2018, pp. 323-327.
- [24] J. Viala, F. Bosselet, G. Claveyrolas, B. Mentzen, J. Bouix, Characterization of two new crystalline phases in the Al-C-Mg system, *European journal of solid state and inorganic chemistry*, 28 (1991) 1063-1070.
- [25] F. Bosselet, B. Mentzen, J. Viala, M. Etoh, J. Bouix, Synthesis, and structure of T<sub>2</sub>-Al<sub>2</sub>MgC<sub>2</sub>, *European journal of solid state and inorganic chemistry*, 35 (1998) 91-99.
- [26] H.-L. Wang, J.-J. Tang, Y.-J. Zhao, J. Du, First-principles study of Mg/Al<sub>2</sub>MgC<sub>2</sub> heterogeneous nucleation interfaces, *Applied Surface Science*, 355 (2015) 1091-1097.
- [27] X. Liu, S. Yin, Z. Zhang, Q. Le, J. Xue, Effect of limestone ores on grain refinement of as-cast commercial AZ31 magnesium alloys, *Trans. Nonferrous Met. Soc. China*, 28 (2018) 1113.
- [28] A. Zhang, Z. Zhao, G. Yin, C. Lin, A novel model to account for the heterogeneous nucleation mechanism of  $\alpha$ -Mg refined with Al<sub>4</sub>C<sub>3</sub> in Mg-Al alloy, *Computational Materials Science*, 140 (2017) 61-69.
- [29] A. Maltais, D. Dube, M. Fiset, G. Laroche, S. Turgeon, Improvements in the metallography of as-cast AZ91 alloy, *Materials Characterization*, 52 (2004) 103-119.
- [30] E. Owen, L. Pickup, I. Roberts, Lattice constants of five elements possessing hexagonal structure, *Zeitschrift für Kristallographie-Crystalline Materials*, 91 (1935) 70-76.

- [31] S. Thimmaiah, Z. Tener, T.N. Lamichhane, P.C. Canfield, G.J. Miller, Crystal structure, homogeneity range and electronic structure of rhombohedral  $\gamma$ -Mn<sub>5</sub>Al<sub>8</sub>, *Zeitschrift für Kristallographie-Crystalline Materials*, 232 (2017) 601-610.
- [32] F. Stein, S.C. Vogel, M. Eumann, M. Palm, Determination of the crystal structure of the  $\epsilon$  phase in the Fe–Al system by high-temperature neutron diffraction, *Intermetallics*, 18 (2010) 150-156.
- [33] L. Palatnik, I. Tananko, Y.G. Bobro, About the nature of  $\epsilon$ -phase in Fe–Al–C alloys, *Kristallografiya*, 9 (1964) 209-212.
- [34] E. Owen, G. Williams, A low-temperature X-ray camera, *Journal of Scientific Instruments*, 31 (1954) 49.
- [35] I. Wood, L. Vočadlo, K. Knight, D.P. Dobson, W. Marshall, G.D. Price, J. Brodholt, Thermal expansion and crystal structure of cementite, Fe<sub>3</sub>C, between 4 and 600 K determined by time-of-flight neutron powder diffraction, *Journal of Applied Crystallography*, 37 (2004) 82-90.
- [36] A. Feldhoff, E. Pippel, J. Woltersdorf, Structure and composition of ternary carbides in carbonfibre reinforced Mg-Al alloys, *Philosophical Magazine A*, 79 (1999) 1263-1277.
- [37] G. Deffrennes, B. Gardiola, E. Jeanneau, G. Mikaelian, P. Benigni, A. Pasturel, A. Pisch, J. Andrieux, O. Dezellus, Synthesis, crystallographic structure and thermodynamic properties of T<sub>2</sub>-Al<sub>2</sub>MgC<sub>2</sub>, *Journal of Solid State Chemistry*, 273 (2019) 150-157.
- [38] T.M. Gesing, W. Jeitschko, The crystal structure and chemical properties of U<sub>2</sub>Al<sub>3</sub>C<sub>4</sub> and structure refinement of Al<sub>4</sub>C<sub>3</sub>, *Zeitschrift für Naturforschung B*, 50 (1995) 196-200.
- [39] V. Grass, Y.I. Ryabkov, B. Goldin, P. Sitnikov, X-Ray diffraction study of aluminum monoxycarbide, *Journal of Structural Chemistry*, 45 (2004) 100-106.
- [40] J. Viala, G. Claveyrolas, F. Bosselet, J. Bouix, The chemical behaviour of carbon fibres in magnesium base Mg-Al alloys, *Journal of materials science*, 35 (2000) 1813-1825.
- [41] H. Springer, A. Kostka, E. Payton, D. Raabe, A. Kaysser-Pyzalla, G. Eggeler, On the formation and growth of intermetallic phases during interdiffusion between low-carbon steel and aluminum alloys, *Acta Materialia*, 59 (2011) 1586-1600.
- [42] M. Sidhu, C. Bishop, M. Kral, Formation of aluminium carbide by cast iron and liquid aluminium interaction, *International Journal of Cast Metals Research*, 27 (2014) 321-328.
- [43] D. Shin, J.-Y. Lee, H. Heo, C.-Y. Kang, Formation procedure of reaction phases in Al hot dipping process of steel, *Metals*, 8 (2018) 820.
- [44] S.-Y. Kwak, J.-G. Yun, J.-H. Lee, D.-I. Shin, C.-Y. Kang, Identification of intermetallic compounds and its formation mechanism in boron steel hot-dipped in Al-7 wt.% Mn alloy, *Coatings*, 7 (2017) 222.



## Figure Captions

Fig. 1. (a) SE image and EDS mapping of T2-Al<sub>2</sub>MgC<sub>2</sub> in AZ91 after 48 h at 700 °C in an Al<sub>2</sub>O<sub>3</sub> crucible. (b) EBSD phase map, experimental Kikuchi pattern and dynamical simulation of T2-Al<sub>2</sub>MgC<sub>2</sub>.

Fig. 2. (a) SE images of typical microstructures of AZ91 in Fe-0.2C and cast iron (Fe-3.6C) crucibles, after isothermal holding at 700 °C for 8 h. (b) Microstructures of the reaction layers formed between AZ91 and Fe-C crucibles containing 0, 0.2, 1.0 and 3.6 wt.% C.

Fig. 3. Reaction layers between AZ91 and Fe-1.0C after 8 h at 700 °C (a) EBSD phase map, experimental Kikuchi patterns from the three carbides, and dynamical simulated patterns with cross correlation coefficients. (b) Schematic of the reaction layer. (c) Successive XRD on the solid surface after (i) α-Mg was selectively etched away, (ii) 1<sup>st</sup> grinding into B2-Al(Fe,Mn) layer and (iii) 2<sup>nd</sup> grinding into α-Fe. The reflections for indexed phase(s) are attached beneath the pattern. \* The peaks are truncated to scale the XRD patterns for a better visual recognition of small peaks. Full details for individual patterns are given in S.I.-Fig. 2-4.

Fig. 4. The reaction layer between AZ91 and Fe-0.2C after 8 h at 700 °C. (a) EDS mapping confirming Mg, Al, C in the Al<sub>2</sub>MgC<sub>2</sub> ternary carbide; Al, Fe, C in κ-AlFe<sub>3</sub>C carbide; Al, Fe in B2-Al(Fe,Mn); and Fe in α-Fe. (b) Schematic of the reaction layer.

Fig. 5. (a-b) Schematic of the reaction layer between AZ91 and Fe-3.6C after 8 h at 700 °C (right), EDS mapping of a graphite flake in the B2 layer which is transforming into Al<sub>2</sub>MgC<sub>2</sub> ternary carbide. (c) EBSD analysis of transforming graphite and Al<sub>2</sub>MgC<sub>2</sub>, and an experimental Kikuchi pattern from the T2-Al<sub>2</sub>MgC<sub>2</sub> with dynamical simulation.

Fig. 6. (a) SEM cross-section image of a κ-AlFe<sub>3</sub>C layer in AZ91 held in 1.0C-steel at 700 °C for 8 h and image at 54° tilt after deep-etching. (b) EBSD phase map and IPF-X map of the κ-AlFe<sub>3</sub>C layer. (c) Measured κ-AlFe<sub>3</sub>C grain size along the layer length and the layer thickness in different experimental conditions.

Fig. 7. (a) EDS mapping, EBSD phase map and schematic for the reaction layer in Fe-0.2C steel crucible held at 700 and 800 °C (4 h) respectively. (b) Diffusion profile for the reaction layer from the Mg side into the steel crucible.

Fig. 8. Isothermal sections through the ternary Al-C-Fe phase diagram at 700, 750 and 800 °C. Single phase regions are black. Two-phase regions contain green tie lines. Three phase tie triangles are yellow. G= graphite. Note that only up to 35 wt. % Al is shown. Solid red circles are the initial steel compositions for κ-AlFe<sub>3</sub>C layer present, unfilled red circles are the initial steel compositions for no κ-AlFe<sub>3</sub>C layer, solid blue diamonds are measured compositions in the diffusion profiles at 700 and 800 °C.

Fig. 9. (a) SE image, EBSD phase map, IPF-Z orientation map and Kikuchi patterns from a twinned T2-Al<sub>2</sub>MgC<sub>2</sub> particle in the Mg bulk; Unit cell wireframe has been plotted from EBSD-measured Euler angles. Orange polygon is digital cross-section of the wireframe model in the plane of the SE image. (b) Pole figures of the {0001}, {11 $\bar{2}$ 0} and {10 $\bar{1}$ 1} families for the same particle, and unit cell orientations plotted from the measured Euler angles. (c) Projection view of trigonal T2-Al<sub>2</sub>MgC<sub>2</sub> along [0001].

Fig. 10.  $\alpha$ -Mg grains in AZ91 held in pure Fe and Fe-3.6C at 700 °C for 8 h and cooled at  $\sim 4$  K/s. (a) Stereo-optical micrographs: transverse section (top) and longitudinal section (bottom). (b) Cross-polarized images from near the center of samples.

Fig. 11. (a) SE image of a T2-Al<sub>2</sub>MgC<sub>2</sub> crystal in the Mg bulk, and EDS mapping; Unit cell wireframe has been plotted from EBSD-measured Euler angles. Orange polygon is digital cross-section of the wireframe model in the plane of the SE image. (b) EBSD phase map and IPF-Z map for the same crystal and the surrounding  $\alpha$ -Mg, experimental Kikuchi patterns of the  $\alpha$ -Mg and the two orientations of T2-Al<sub>2</sub>MgC<sub>2</sub> highlighting parallel planes. (c) Pole figures for the {0001}, {11 $\bar{2}$ 0} and {10 $\bar{1}$ 1} families of  $\alpha$ -Mg and T2-Al<sub>2</sub>MgC<sub>2</sub>, and unit cell orientations from the EBSD-measured Euler angles. (d) Projection views of hexagonal  $\alpha$ -Mg and trigonal T2-Al<sub>2</sub>MgC<sub>2</sub> along [0001].

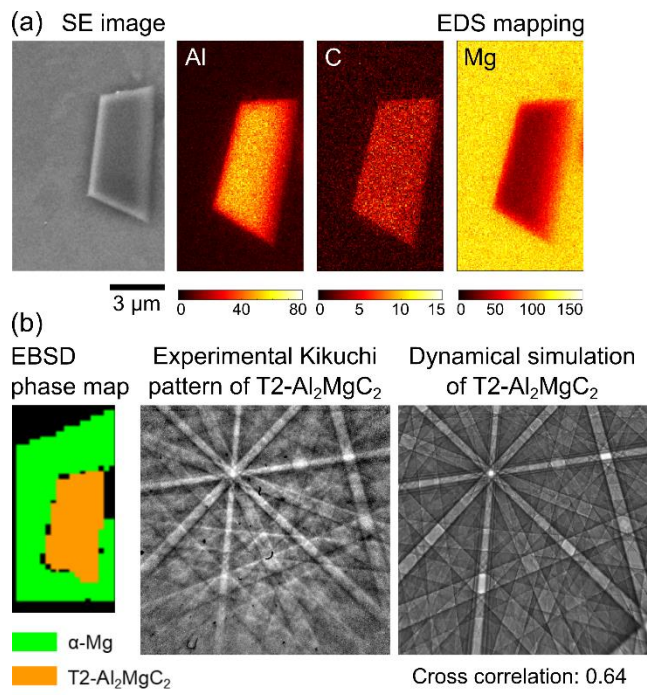


Fig. 12. (a) SE image and EDS mapping of T2-Al<sub>2</sub>MgC<sub>2</sub> in AZ91 after 48 h at 700 °C in an Al<sub>2</sub>O<sub>3</sub> crucible. (b) EBSD phase map, experimental Kikuchi pattern and dynamical simulation of T2-Al<sub>2</sub>MgC<sub>2</sub>.

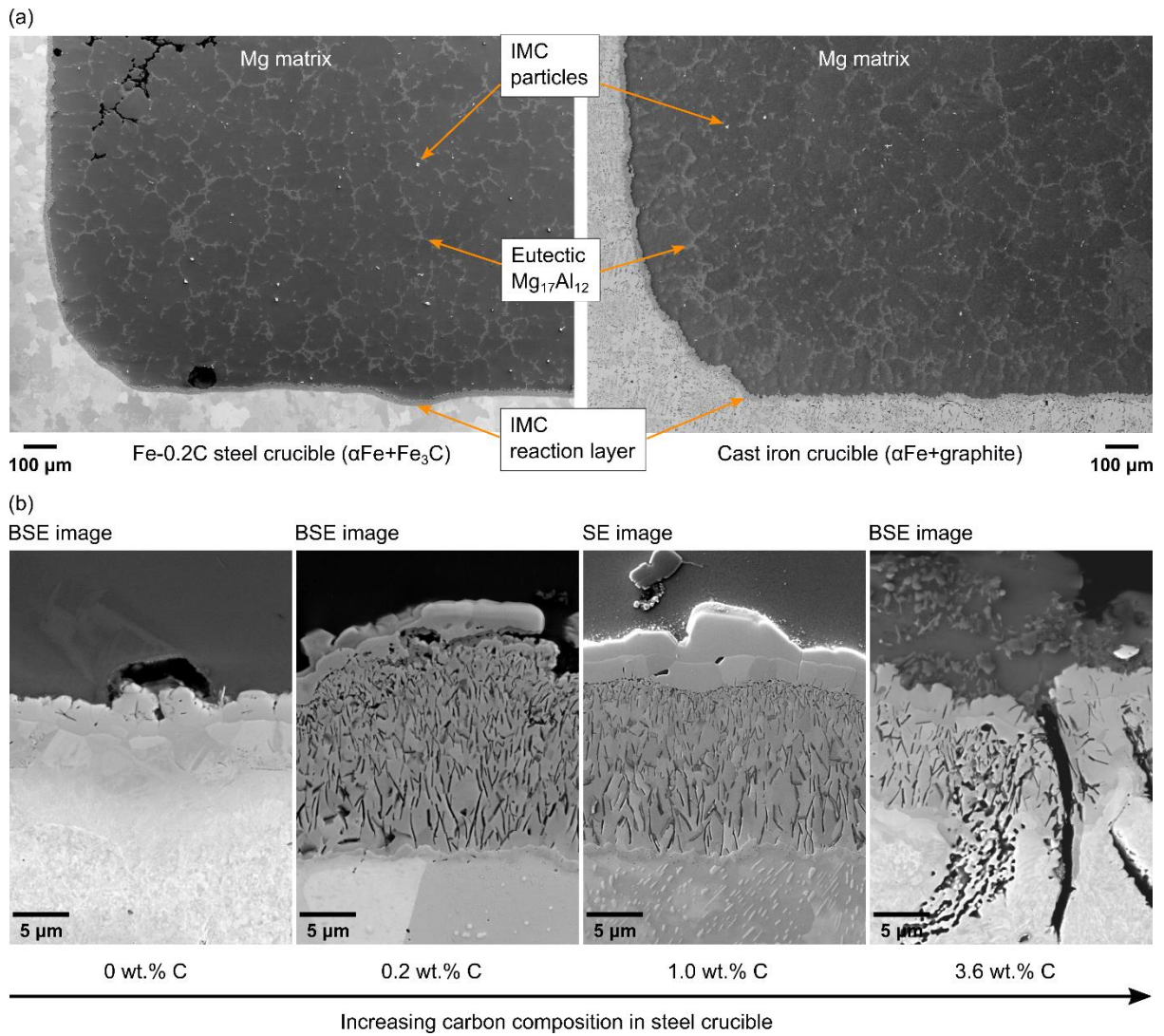


Fig. 13. (a) SE images of typical microstructures of AZ91 in Fe-0.2C and cast iron (Fe-3.6C) crucibles, after isothermal holding at 700 °C for 8 h. (b) Microstructures of the reaction layers formed between AZ91 and Fe-C crucibles containing 0, 0.2, 1.0 and 3.6 wt.% C.

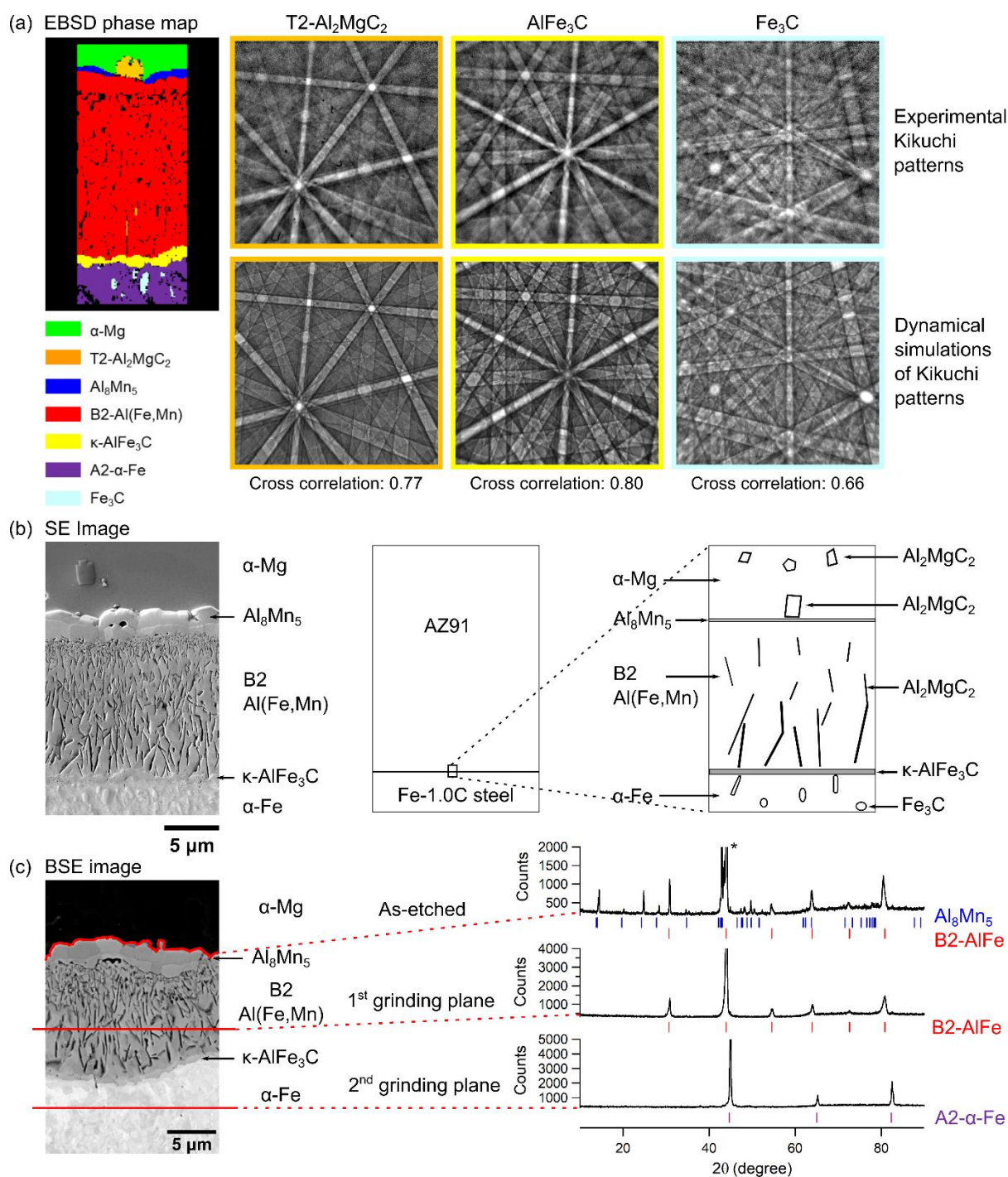
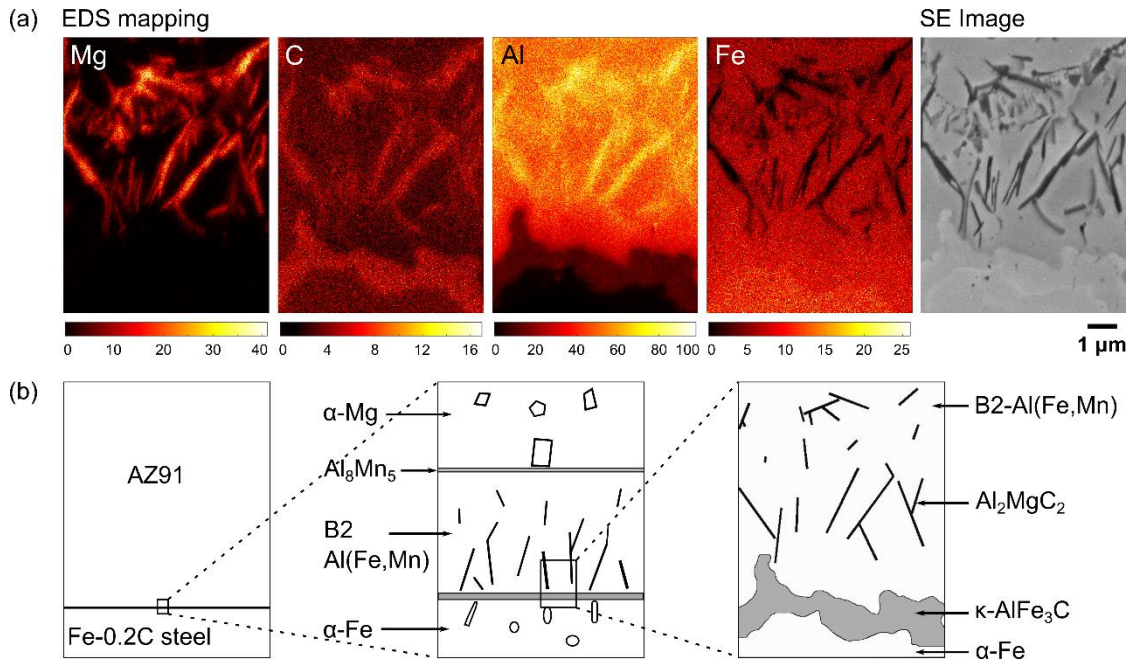


Fig. 14. Reaction layers between AZ91 and Fe-1.0C after 8 h at 700 °C (a) EBSD phase map, experimental Kikuchi patterns from the three carbides, and dynamical simulated patterns with cross correlation coefficients. (b) Schematic of the reaction layer. (c) Successive XRD on the solid surface after (i)  $\alpha$ -Mg was selectively etched away, (ii) 1<sup>st</sup> grinding into B2-Al(Fe,Mn) layer and (iii) 2<sup>nd</sup> grinding into  $\alpha$ -Fe. The reflections for indexed phase(s) are attached beneath the pattern. \* The peaks are truncated to scale the XRD patterns for a better visual recognition of small peaks. Full details for individual patterns are given in S.I.-Fig. 2-4.



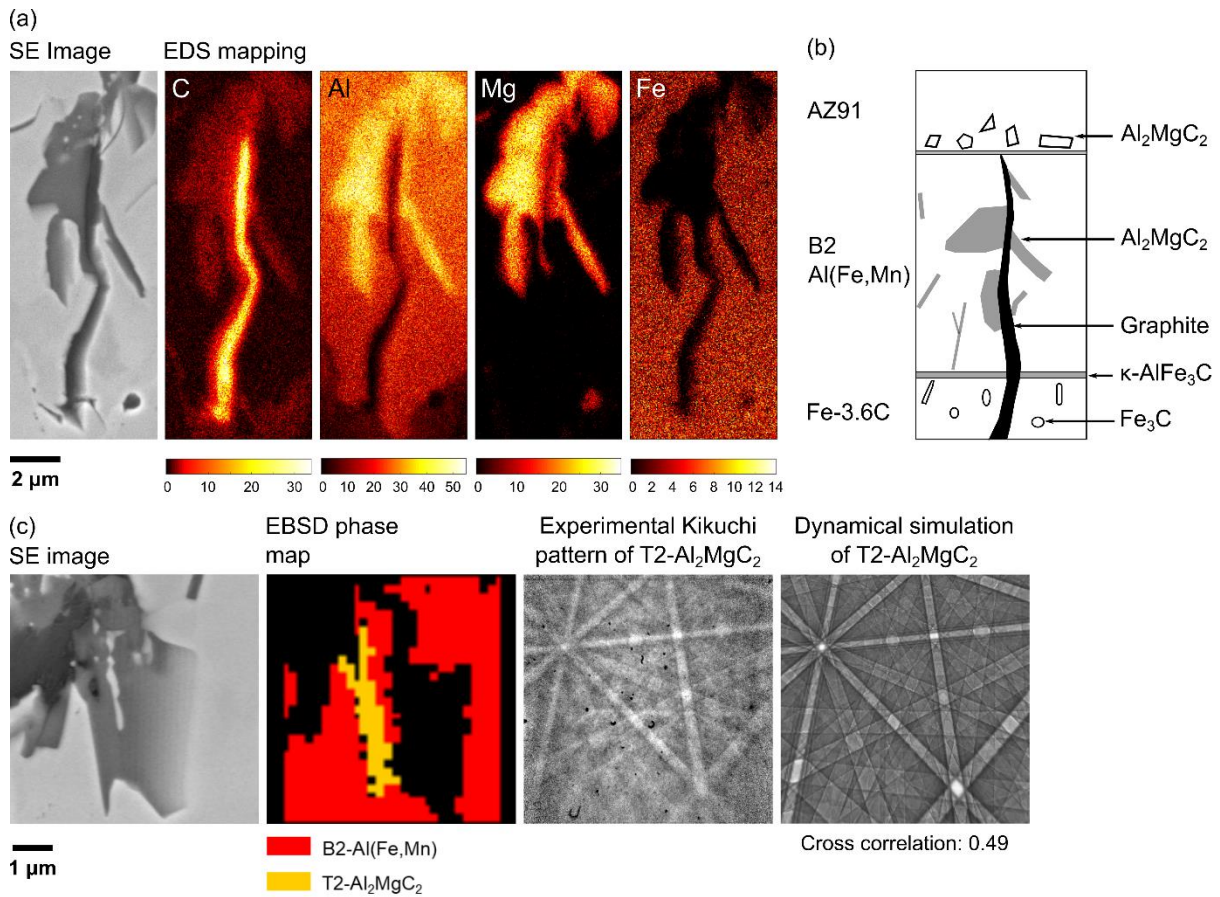


Fig. 16. (a-b) Schematic of the reaction layer between AZ91 and Fe-3.6C after 8 h at 700 °C (right), EDS mapping of a graphite flake in the B2 layer which is transforming into  $\text{Al}_2\text{MgC}_2$  ternary carbide. (c) EBSD analysis of transforming graphite and  $\text{Al}_2\text{MgC}_2$ , and an experimental Kikuchi pattern from the T2- $\text{Al}_2\text{MgC}_2$  with dynamical simulation.

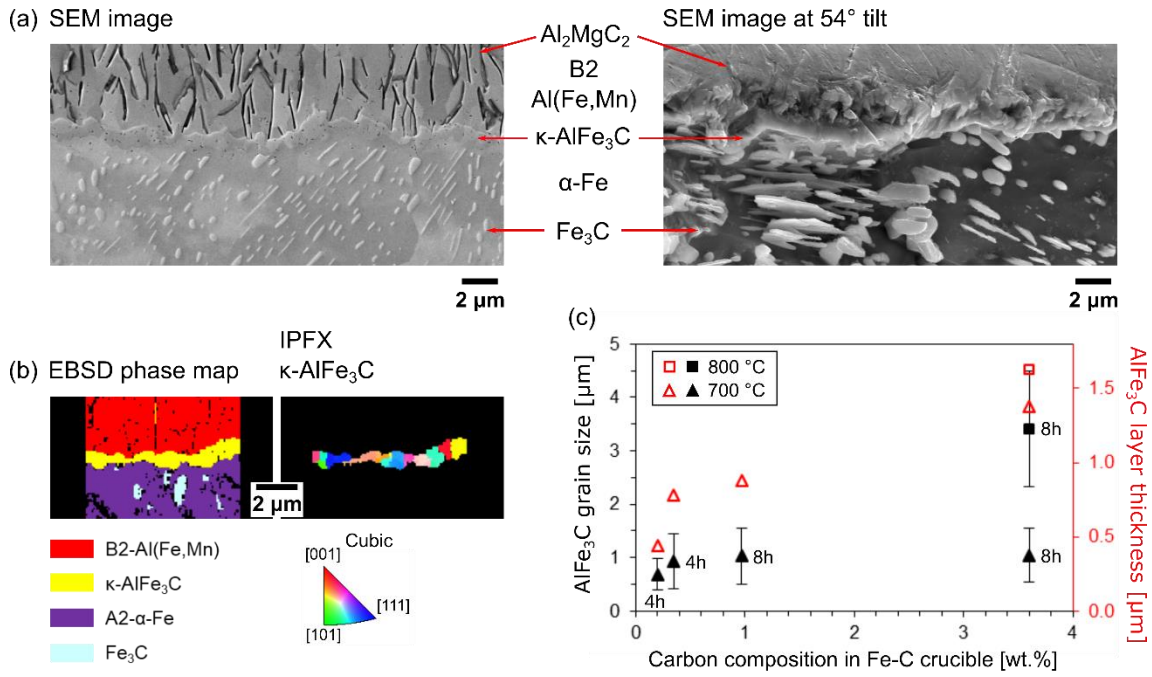


Fig. 17. (a) SEM cross-section image of a  $\kappa$ -AlFe<sub>3</sub>C layer in AZ91 held in 1.0C-steel at 700 °C for 8 h and image at 54° tilt after deep-etching. (b) EBSD phase map and IPF-X map of the  $\kappa$ -AlFe<sub>3</sub>C layer. (c) Measured  $\kappa$ -AlFe<sub>3</sub>C grain size along the layer length and the layer thickness in different experimental conditions.



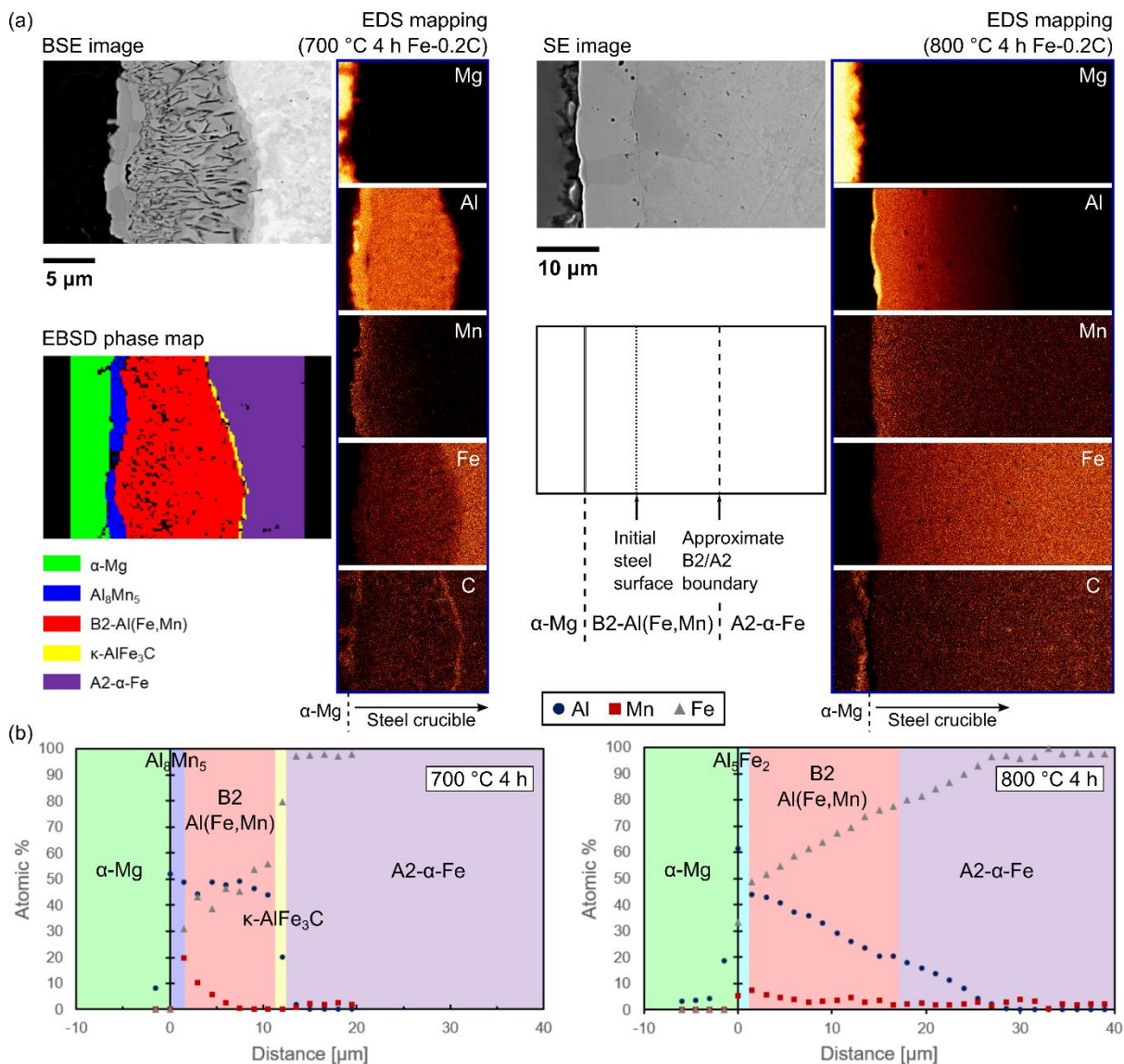


Fig. 18. (a) EDS mapping, EBSD phase map and schematic for the reaction layer in Fe-0.2C steel crucible held at 700 and 800 °C (4 h) respectively. (b) Diffusion profile for the reaction layer from the Mg side into the steel crucible.

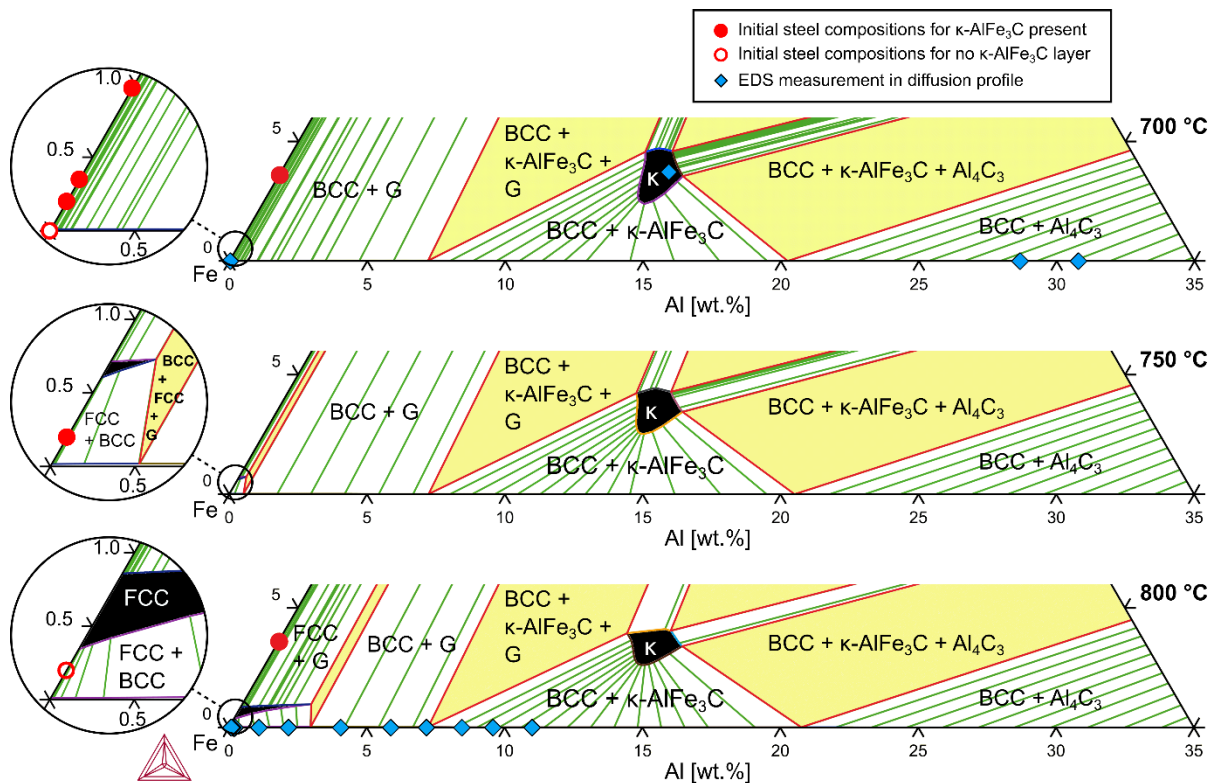


Fig. 19. Isothermal sections through the ternary Al-C-Fe phase diagram at 700, 750 and 800 °C. Single phase regions are black. Two-phase regions contain green tie lines. Three phase tie triangles are yellow. G= graphite. Note that only up to 35 wt. % Al is shown. Solid red circles are the initial steel compositions for  $\kappa$ -AlFe<sub>3</sub>C layer present, unfilled red circles are the initial steel compositions for no  $\kappa$ -AlFe<sub>3</sub>C layer, solid blue diamonds are measured compositions in the diffusion profiles at 700 and 800 °C.

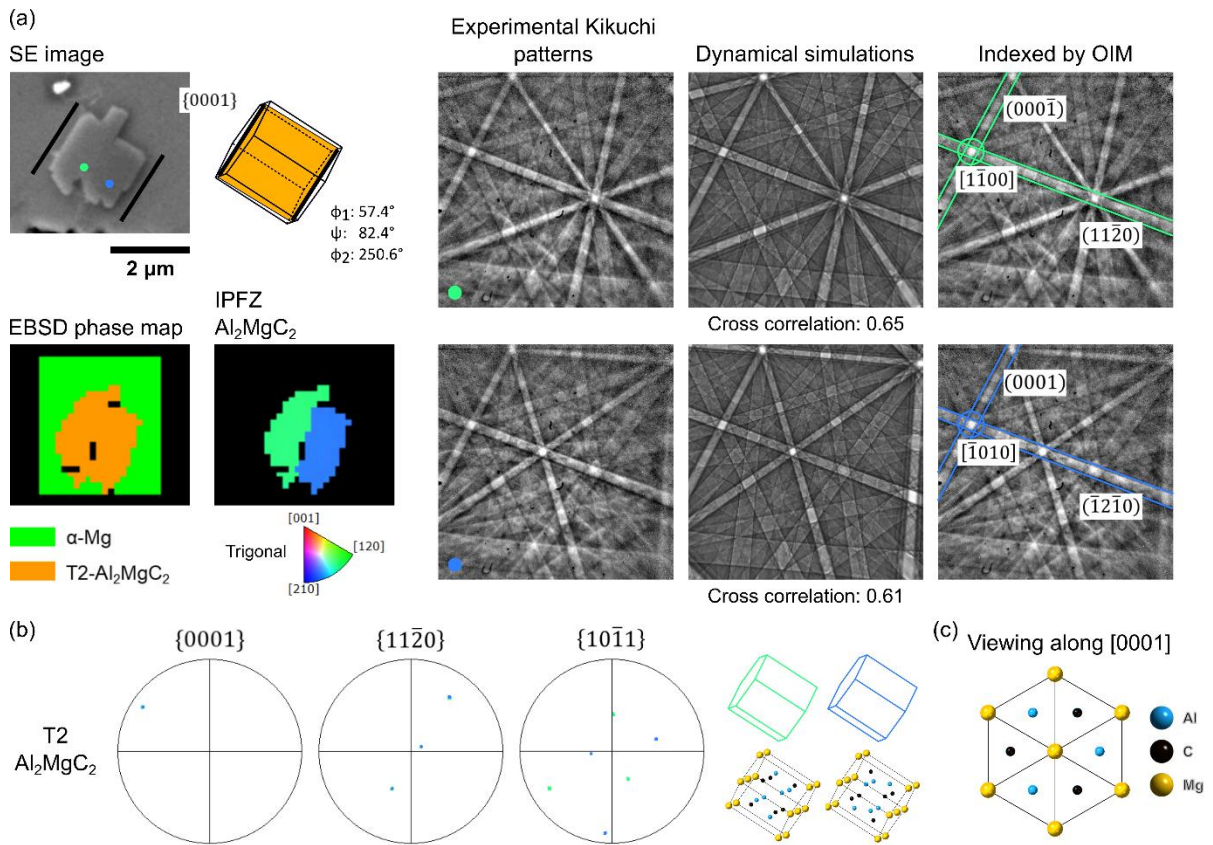


Fig. 20. (a) SE image, EBSD phase map, IPF-Z orientation map and Kikuchi patterns from a twinned T2- $\text{Al}_2\text{MgC}_2$  particle in the Mg bulk; Unit cell wireframe has been plotted from EBSD-measured Euler angles. Orange polygon is digital cross-section of the wireframe model in the plane of the SE image. (b) Pole figures of the  $\{0001\}$ ,  $\{11\bar{2}0\}$  and  $\{10\bar{1}1\}$  families for the same particle, and unit cell orientations plotted from the measured Euler angles. (c) Projection view of trigonal T2- $\text{Al}_2\text{MgC}_2$  along  $[0001]$ .

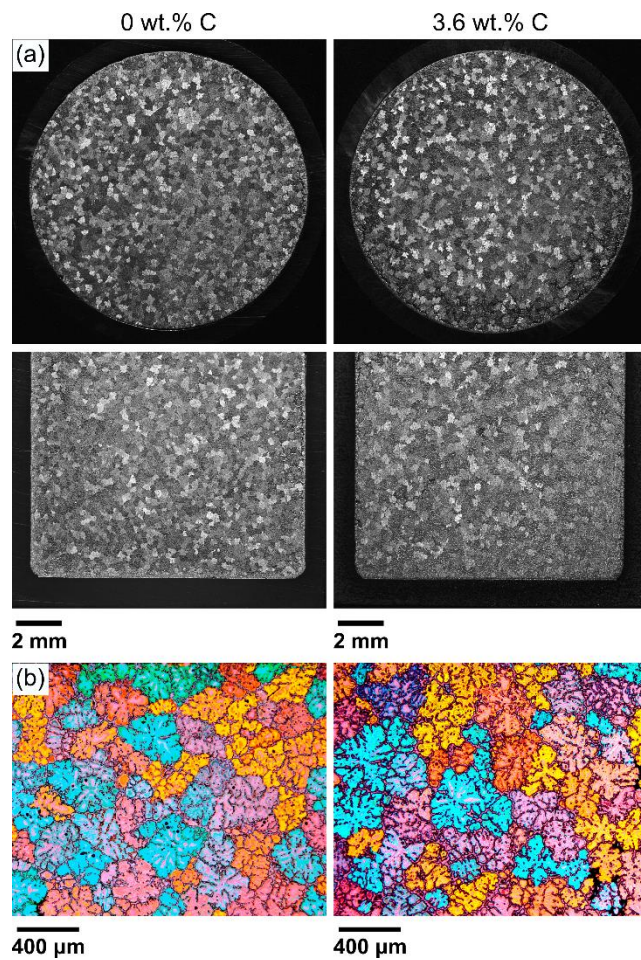


Fig. 21.  $\alpha$ -Mg grains in AZ91 held in pure Fe and Fe-3.6C at 700 °C for 8 h and cooled at  $\sim$ 4 K/s. (a) Stereoptical micrographs: transverse section (top) and longitudinal section (bottom). (b) Cross-polarized images from near the center of samples.

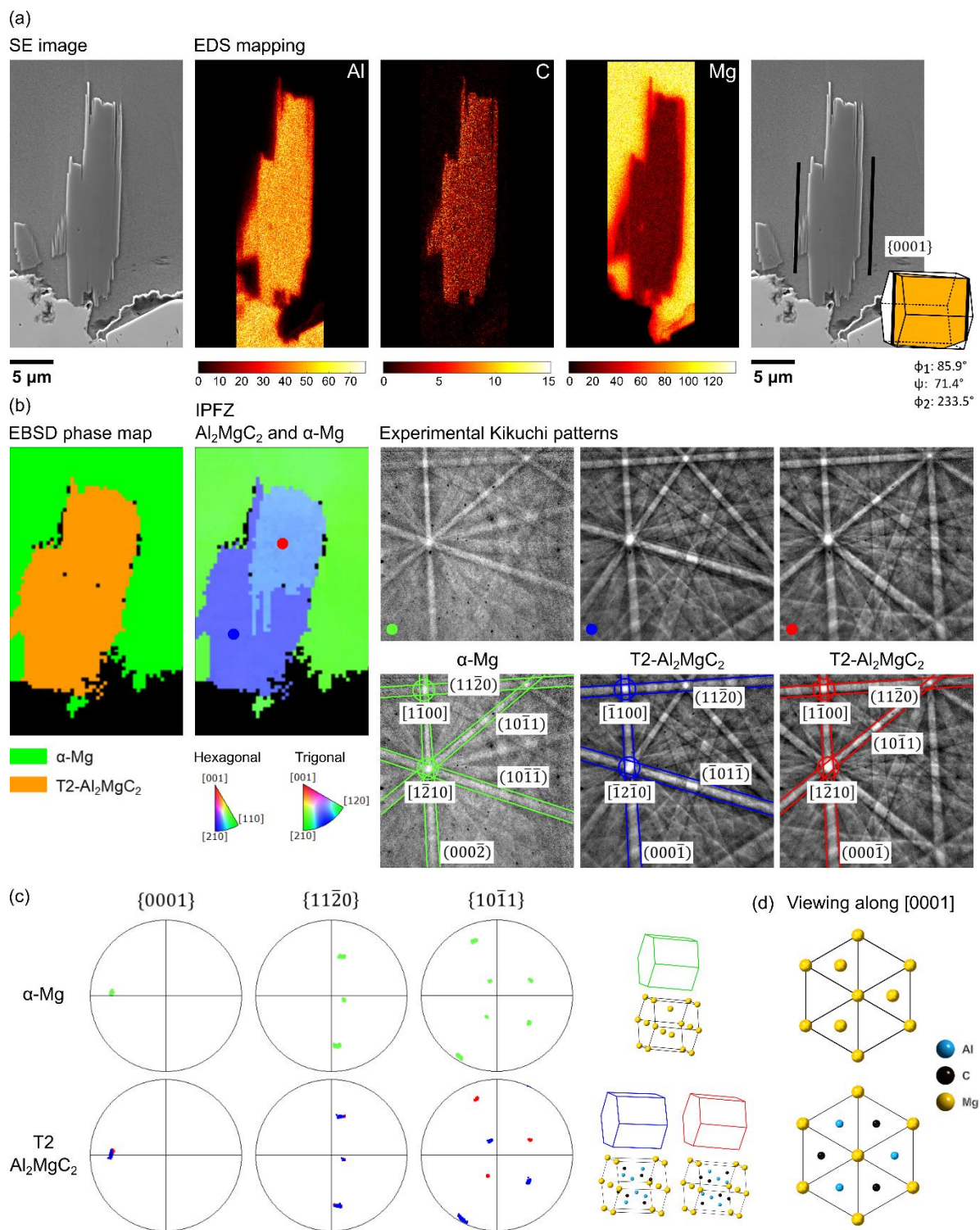


Fig. 22. (a) SE image of a T2-Al<sub>2</sub>MgC<sub>2</sub> crystal in the Mg bulk, and EDS mapping; Unit cell wireframe has been plotted from EBSD-measured Euler angles. Orange polygon is digital cross-section of the wireframe model in the plane of the SE image. (b) EBSD phase map and IPF-Z map for the same crystal and the surrounding  $\alpha$ -Mg, experimental Kikuchi patterns of the  $\alpha$ -Mg and the two orientations of T2-Al<sub>2</sub>MgC<sub>2</sub> highlighting parallel planes. (c) Pole figures for the {0001}, {1120} and {1011} families of  $\alpha$ -Mg and T2-Al<sub>2</sub>MgC<sub>2</sub>, and unit cell orientations from the EBSD-measured Euler angles. (d) Projection views of hexagonal  $\alpha$ -Mg and trigonal T2-Al<sub>2</sub>MgC<sub>2</sub> along [0001].